next-CSP

High Temperature concentrated solar thermal power plant with particle receiver and direct thermal storage

European funded project - Grant Agreement number 727762

Deliverable D2.1

WP2 – Assessment of solar fields for high temperature solar power tower

Deliverable D2.1. Report on Themis solar field performance

Date of Delivery:

Deliverable Authors and Contributors: B. Grange, G. Flamant, W. Baltus, A. Perez, C. Caliot, P.H. Defieux, Y. Volut

Document identifier: next-CSP-WP2-D2.1

Deliverable leader	CNRS
Deliverable contributors	CNRS
Related work package	WP2
Authors and contributors	B. Grange, G. Flamant, W. Baltus, A. Perez, C. Caliot, P.H. Defieux, Y. Volut
Due date of deliverable	September 30th 2018
Actual submission date	November 29th 2018
Approved by	Coordinator
Dissemination level	Public
Website	http://next-csp.eu/
Call	H2020-LCE-07-2016 Developing the next generation technologies of renewable electricity and heating/cooling Specific Challenge: Concentrated Solar Power
Project number	727762
Instrument	Research & Innovation Actions
Start date of project	01/10/2016
Duration	48 months

Table of content

1. Introduction and objectives of D2.1

Measurement of the concentrated solar flux distribution at the aperture of a solar receiver is essential to predict the thermal power transferred to the fluid (along the tubes in our case), to avoid hot spots, and to determine the incident solar power on the absorber surface, hence the thermal efficiency of the receiver. During the execution of T2.1, the first step was to adjust the mirrors' canting of heliostats presenting a double focal spot in order to predict accurately the flux distribution by running ray-tracing simulations of the solar field. The second step was to develop a tool for controlling the flux distribution on the solar receiver in order to extend its lifetime by avoiding hot spots. Therefore, an aiming point strategy tool was developed by coupling a convolution-projection optical model and a ray-tracing software.

The validation of the optical simulation and aiming strategy requires a solar flux measurement device. Therefore, the main objectives of D2.1 are to define the solar flux measurement device and to provide first results of experimental data.

This deliverable summarizes the first two steps of the work done on mirrors canting and on aiming point strategy and details the development of the flux distribution measurement device (moving bar) designed, constructed and tested in the framework of T2.1.

2. Canting adjustment of heliostats' modules

Thirty heliostats of the Themis solar field had canting problems (wrong orientation of mirrors leading to double focal spot) which induced a complex control of the flux distribution on the solar receiver. Therefore, an optimization procedure was established to fit simulated heliostat flux distributions to those captured on a white target. Based on a convolution-projection optical model, a deterministic algorithm – named DIRECT – has been implemented. This method allowed adjusting the canting of the thirty heliostats' mirrors.

Figure 1 shows the canting adjustment of heliostat C06 and Figure 2 shows a picture of the procedure to adjust the mirrors using a bucket truck. This operation needs at least two persons to be executed.

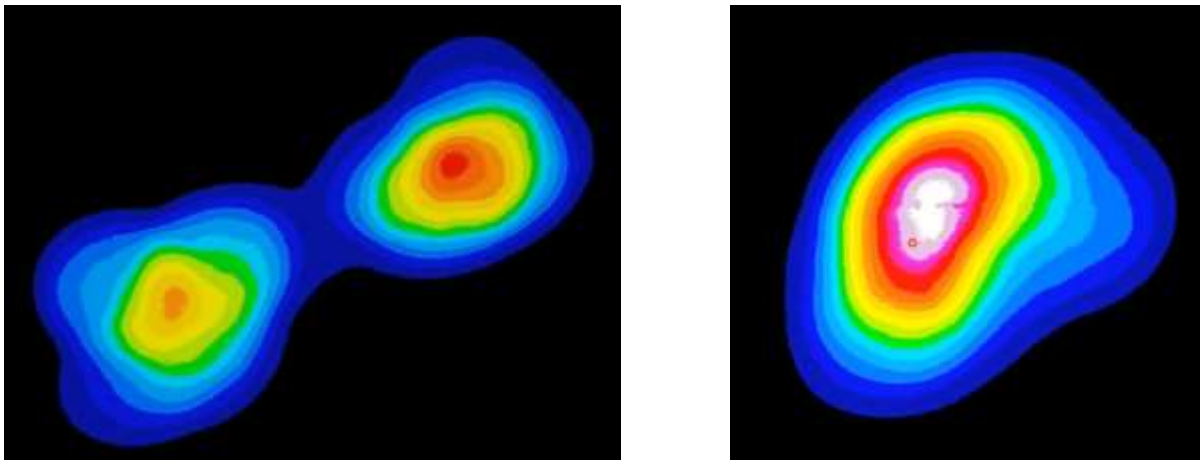

Figure 1. Flux distribution of heliostat C06 before (left) and after (right) canting readjustment

Figure 2. Adjustment of a heliostat's mirrors using a bucket truck

3. Aiming point strategy on the Next-CSP receiver

As shown in Figure 3, the Next-CSP solar receiver consists in 40 vertical tubes (3m-long) in which particles flow upwards.

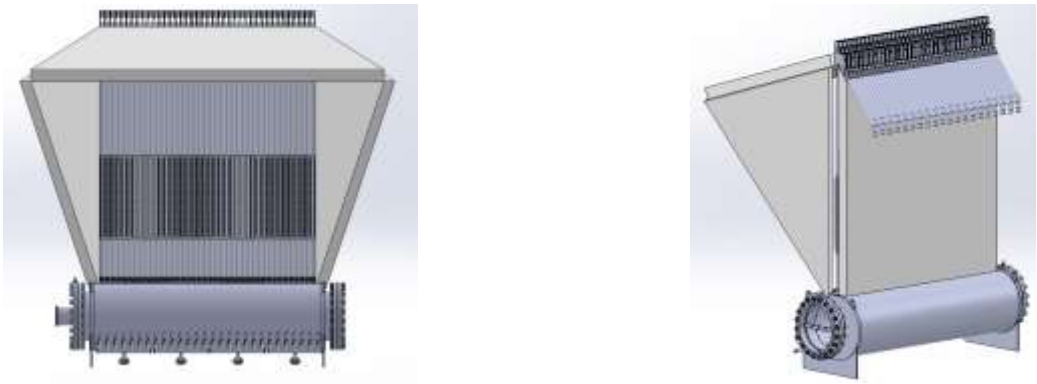

Figure 3. Receiver front (left) and back (right) view with its 40 tubes and cavity made of refractory panels

Aiming Point Strategy (APS) is essential to heat up uniformly the particles in all the 40 tubes and thus, to operate the solar receiver and to extend its lifetime. APS is investigated by applying the TABU meta-heuristic method [1] associated with the convolution-projection optical model UNIZAR [2]. The APS is carried out on an aperture plane located on the mid-plane of the tubes. A 3 m x 3 m aperture plane is considered and 25 points are defined as shown in Figure 4.

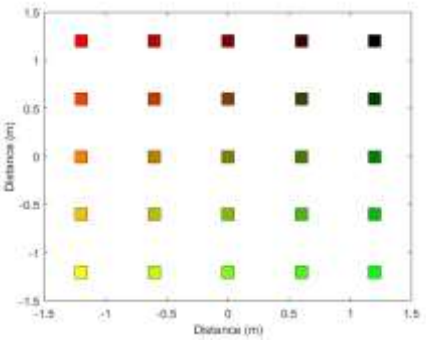

Figure 4. 5 x 5 grid of aiming points

The cost function is the root-mean-square deviation between an objective normalized flux distribution and the normalized simulated flux distribution. The spillage loss (SL) is defined as:

$$SL = 1 - \frac{Q_{rec}}{Q_{ref}}$$

Where Q_{rec} and Q_{ref} are the power intercepted by the 3 m x 3 m aperture with and without APS (single aiming point for the entire heliostat field), respectively. With APS, the spillage loss (SL) must be monitored and kept below a certain threshold. In our case, the SL is limited to a maximum of 30% in the TABU search.

The objective normalized flux distribution is obtained by applying a typical Gaussian distribution horizontally and the following normalized surge function vertically:

$$y = \left(\frac{x}{x_{peak}}\right)^{x_{peak}.b} exp\left(b\left(x_{peak} - x\right)\right)$$

Where x_{peak} is the vertical location of the maximum flux density and b is a parameter that allows modifying the shape of the distribution (flat or sharp).

Figure 5 shows a typical objective normalized flux distribution with a schematic view of the tubes' location. The tubes are 50.8 mm outer diameter and there is a 14.2 mm gap between each tube. For this reference case, the maximum flux distribution is located at middle height of the tube (x_{peak} = 1.5 m), the standard deviation of the Gaussian distribution σ^2 and the parameter b are set to 12 and 0.5, respectively.

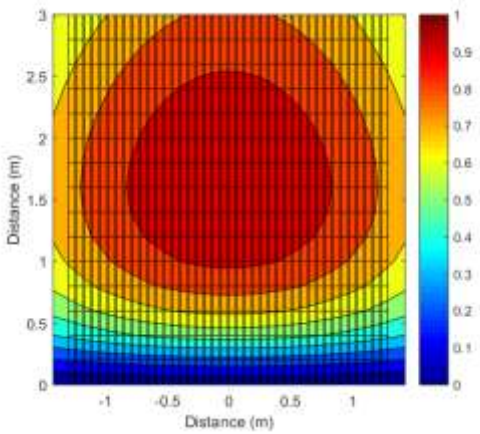

Figure 5. Typical objective normalized flux distribution on the target located at the mid-plane of the tubes and schematic view of the receiver tubes

Results of APS are introduced into *Solstice*, a new open-source ray-tracing software developed by the CNRS-PROMES laboratory and Meso-Star SAS [3]. *Solstice* uses the YAML (Yet Another Markup Language) language to create geometries. It is designed to handle efficiently complex solar facilities. It can import CAD model and therefore simulate ray's path in real geometry. Influence of the variation of surface optical properties with wavelength can also be taken into account.

In these simulations, the tubular geometry of the receiver and the different refractory panels are considered. Indeed, as shown in Figure 3, a refractory panel is located behind the tubes to reflect the concentrated light passing through the gaps between the tubes onto the back of the tubes. In addition, a divergent half cavity made of refractory panel is positioned around the receiver to improve the thermal efficiency. The angles of the cavity panels result from the position of the most Eastern, Western and Northern heliostats of the solar field.

Figure 6 presents results in the ray-tracing software without and with APS.

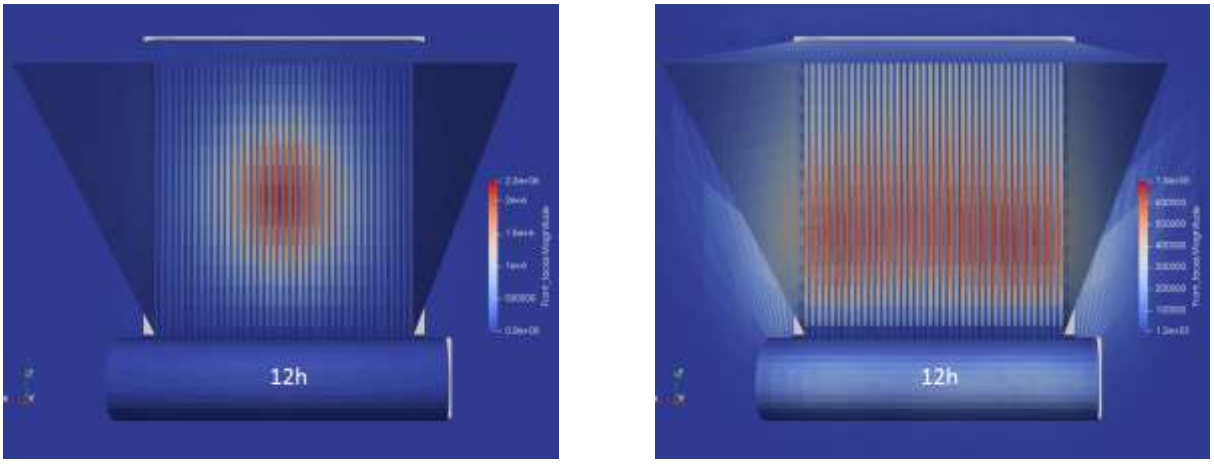

Figure 6. Flux distribution on the tubes without APS (left) and with APS (right)

Simulations confirmed that an aiming strategy leads to a considerable decrease of the highest flux density on the receiver tubes, hence the highest temperature on the receiver. Consequently, the thermal gradients on the tubes are attenuated. However, simulations revealed that reducing the maximum flux density from 2.3 MW/m² down to 700 kW/m² results in the total incident power drops from almost 4.5 MW down to 3 MW (Figure 7) because of spillage.

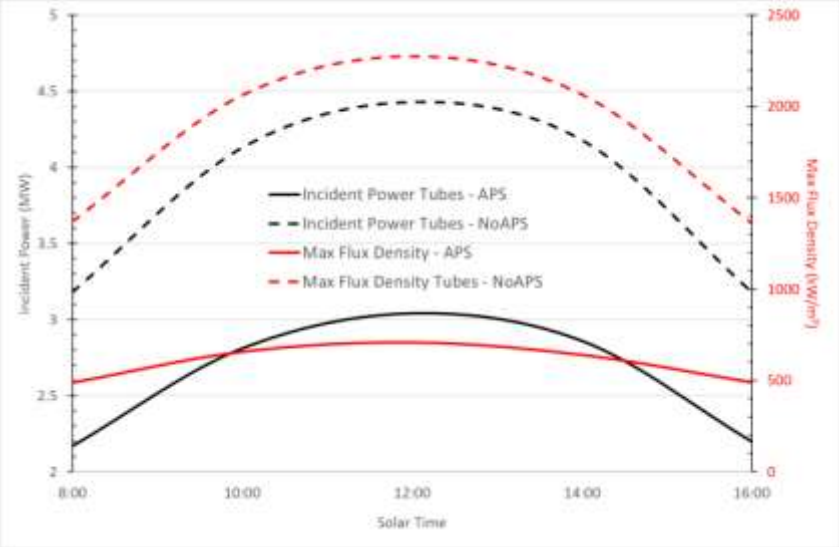

Figure 7. Influence of APS on the incident power and maximum flux density

4. Description of the flux measurement device

The measurement of concentrated solar flux and flux mapping at the aperture of a central receiver during the testing of this component and later during the operation of the plant provides very helpful information for research purposes and to the operator. The knowledge of the solar power entering into the receiver, the implementation of an aiming point strategy and more generally the anticipated detection of potential hot spots onto the solar absorber surface are greatly facilitated when these data are available in real time or at least with a short delay. The method is based on the processing of images of the receiver aperture taken by a CMOS camera when a moving target scans the aperture plane. Our approach emphasizes the issue of the reconstruction of the flux distribution from the sequence of images of the moving bar. A fast response heat flux sensor installed on the moving bar carries out the calibration of the grey scale reconstructed image.

4.1 Fast CMOS camera

To carry out the measurement of concentrated solar flux and flux mapping at the aperture of the receiver, a CMOS camera (Basler, sensor CMOS Sony IMX174, 1920*1200, monochrome) with a high picture rate (163 f/s) and a lens are located on the ground inside a shelter in the center of the solar field.

Figure 8. Installation of the CMOS camera and picture of the Next-CSP receiver frame

The camera associated to the lens presented in Figure 8 offers a 16-bit dynamic and a precise resolution of 2.34 x 2.34 mm per pixel. Neutral filters are used to damp the light intensity.

4.2 Moving bar

The moving bar is installed on a carriage fixed on a chain driven by a motor (Figure 9). A ±200 mm adjustment is possible in two directions in order to make sure that the moving bar is located in front of the cavity aperture.

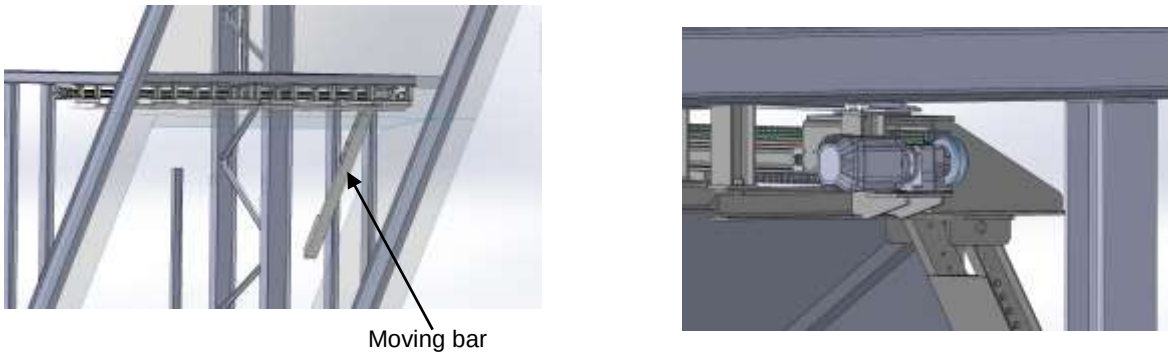

Figure 9. Picture of the moving bar translation system

The moving bar travels from East to West or West to East at a nominal speed of 2 m/s. When the moving bar travels, the above-mentioned CMOS camera takes pictures at a rate of around 40 FPS. This results in a total number of pictures of around 160 pictures that are post-processed in order to rebuild the whole intensity distribution. The moving bar has a central white stripe of 20 cm and two black stripes on each side (post-processing detailed in the section 3) to make the post-processing possible.

Three thermocouples are installed at the back of the moving bar to monitor its temperature and make sure it does not reach the maximal temperature that the acquisition system can handle.

4.3 Fast-response heat flux sensor

The transient flux measured by a fast response flux gauge attached to the target is used for calibrating the images. The flux gauge is the heat flux micro-sensor model HFM 6 supplied by Vatell Corp. The heat flux sensor is Rh/Pt-Rh thermopile 4 mm in diameter, covered with Pyromark® film to achieve solar absorbance of 94%. The response time claimed by Vatell is 17 µs to 300 µs. The sensitivity is temperature dependent, with a minimum value of 3.2 µV/W.cm² at ambient temperature. The accuracy is ± 3% over the whole range of measurement. The gauge is equipped with a Pt-100 resistance thermal sensor, which measures the temperature of the face of the heat flux sensor submitted to concentrated solar radiation. This signal is processed to correct

the actual gain of the heat flux sensor. An amplifier receives both flux and temperature low voltage signals and delivers x1000 and x500 high voltage signals, respectively. Finally, a high-speed (100 kHz) A/D converter and data acquisition system ADDI DATA MSX-E3011 is used to record transient signals during the scanning of the aperture. The flux gauge is located into the center of the target.

4.4 Pictures of the installation

Scaffolding to hang the flux measurement system

Flux measurement system installed (moving bar surrounded in red)

Acquisition system installed at the back of the moving bar

Welding of the metallic protection

Metallic protection lifted and installed to block the concentrated radiation

View of the Next-CSP aperture with metallic protection

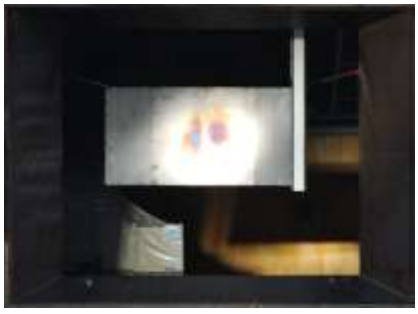

Moving bar in motion (1)

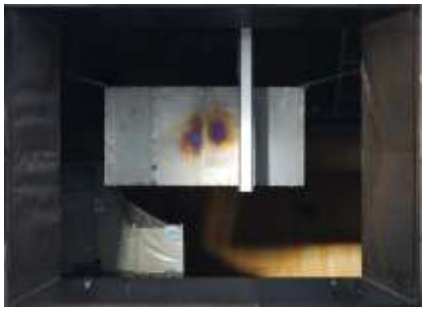

Moving bar in motion (2)

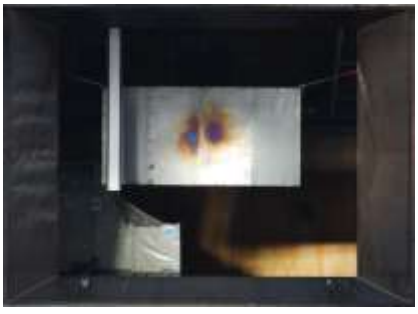

Moving bar in motion (3)

5. Data processing

5.1 Measurement output

For each series of measurement, the outputs are:

- A sequence of images in the ".tiff" format (around 240 images)
- A csv file giving the flux measurement versus time

- Data about the DNI

5.2 Required outputs from data processing

The required outputs through the algorithm are:

- A picture of the flux distribution at the cavity aperture
- The power entering the aperture
- The solar concentration ratio

5.3 Data processing

The data processing is composed of five steps:

- Processing of raw images to eliminate or reduce measurement noise and bias
- Detection of the bar in each image
- Statistic approach for mapping the grey values
- Calibration of grey scale using heat flux sensor data
- Total input power into the cavity

5.3.1 Processing of raw images

The image processing requires the capture of a sequence of black images (same area of interest on the CMOS matrix, same gain and shutter speed, but with the tap on), and a sequence of flat-field images (tap replaced by a uniform brightness source). The median average of each sequence is applied and results in a single black image and flat-field image named I_{black} and I_{flat}, respectively.

The black image contains the electronic bias and noise generated by the A/D converter while the flat-field image contains the noise and distortion generated by each pixel when discharging their current and the optical defaults resulting from dust and scratches possibly remaining on the lens.

Each raw image of the sequence I_{raw} taken during the scanning is converted into a “net” image I_{net} using the following equation:

$$I_{net} = \frac{I_{raw} - I_{black}}{I_{flat} - I_{black}}$$

The Peak Signal to Noise Ratio (PSNR) is calculated for each image:

$$PSNR = 10log_{10}\left(\frac{1}{rms(I_{raw} - I_{net})}\right)$$

Where $rms(I_{raw} - I_{net})$ is the root mean square deviation between the raw and the net image.

A value of PSNR above 40 guarantees that the noise and the bias are correctly removed.

5.3.2 Detection of the bar

The last image of the sequence is taken as background image I_{back}, since the bar is returned to the garage position and does not appear in the frame anymore. The background is subtracted from each “net” image, making a final sequence of images named “corrected” images I_{corr}:

$$I_{corr} = I_{net} - I_{back}$$

In the corrected image I_{corr}, the contrast between the bar and the surrounding significantly increases. The background is currently a metallic protection (and will be the Next-CSP solar receiver later) irradiated by the concentrated solar flux, it is almost unchanged during the scanning. However, the small correction of the orientation of the heliostats due to the tracking and the shadow of the bar on the surface of the protection in the back result in fuzzy position of the bar edges in the corrected image.

Two methods are compared for accurately detecting the position of the bar: the time derivative approach and the spatial derivative approach.

In the time derivative approach, the derivative between two consecutive corrected images is calculated for each pixel. The two edges of the bar appear in the region where the derivative is maximum. However, the detection is poor when the bar is in a dark region.

In the spatial derivative approach, the derivative between two neighbor pixels on a horizontal line in a same corrected image is calculated. The two black bands on the edges of the bar yield a big change in brightness and thus a better detection than the one obtained with the time derivative approach. Two particular cases are the situations in which only one edge is detected because the bar is partly present: at the beginning and at the end of the scanning. In these cases, the direction of the movement of the bar indicates in which region of the image the bar is.

In conclusion, the detection based on the spatial derivative approach appears as more reliable and more accurate than the time derivative. Although it is slower in execution, the spatial derivative is finally selected. The sequence of corrected images is restricted to the images taken during the one-way or during the return movement. Therefore, the direction of the bar is known. In addition, the calibration using the flux gauge signal is much better, as it is explained later.

The corrected images are normalized using the maximum and the minimum values of each pixel in all the sequence:

$$I_{corr-n} = 2\frac{I_{corr} - Min_{pix-all}}{Max_{pix-all} - Min_{pix-all}} - 1$$

The gradient along the horizontal axis (x) is calculated according to the spatial derivative approach:

$$I_{grad-x} = grad(I_{corr-n})$$

The gradient is normalized using the maximum and the minimum values of gradient in all the sequence:

$$I_{grad-x-n} = 2\frac{I_{grad-x} - Min_{grad-x-all}}{Max_{grad-x-all} - Min_{grad-x-all}} - 1$$

Finally, the average value of the normalized gradient along each column is calculated:

$$Mean_{grad-x-n} = mean_y\left(I_{grad-x-n}\right)$$

By doing this, the 2D image is converted into a single horizontal line represented by the mean normalized gradient $Mean_{grad\text{-}x\text{-}n}$. From this stage, the detection of the bar on the horizontal axis consists in detecting the position(s) of the maximum (positive) and minimum (negative) values of $Mean_{grad\text{-}x\text{-}n}$ by comparison with two thresholds. Two extrema are detected when the bar is entirely visible: $min(Mean_{grad\text{-}x\text{-}n})$ and $max(Mean_{grad\text{-}x\text{-}n})$, at the positions X_{min} and X_{max} respectively. They are assumed to be the limits between the black bands and the central white area of the bar. Only one extremum is detected when the bar is partly shadowed on one side of the window.

A margin of error ΔX is introduced in order to reject the black bands and to eliminate any deviation due to the shadow of the bar projected on the background. This margin of error must remain

smaller than half of the overlapping of the bar in two consecutive images. The position of the bar is situated within the interval [X_{min} + ΔX ; X_{max} - ΔX].

This algorithm of detection comprises two parameters set by the user: threshold and margin of error. It has been tested in many situations, it offers high reliability, reproducibility and robustness. The algorithm is implemented in a software tool dedicated to the data processing. Figure 10 shows an example of the bar detection algorithm as it is implemented in the software.

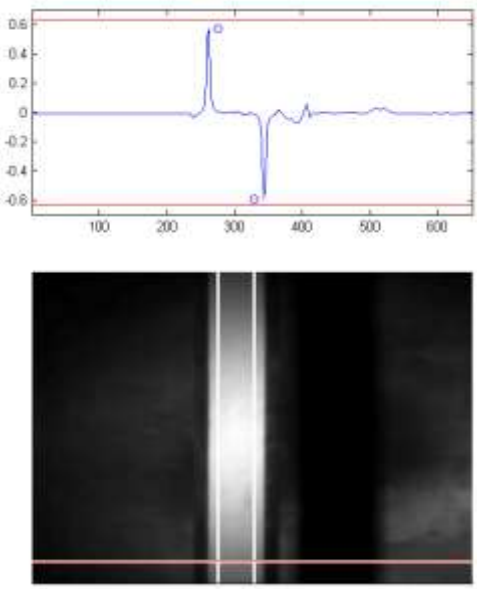

Figure 10. Detection of the bar using the normalized gradient averaged per column (top) and the application of margin of error (bottom)

5.3.3 Statistic approach for mapping the grey values

In each corrected image, the data outside of the portion of bar, as it was detected, is useless. It was set to zero. The remaining useful information is the brightness of the bar, expressed as grey values of pixels. By doing this, the sequence of corrected images is converted into a stack of useful images. Because of the overlapping of the bar in two successive images, several grey values are available at a given pixel position. A statistical analysis of these values yields a good estimate of the value that is finally attributed to this pixel in the map. For each pixel position p in the map we proceed as follows: the n values available at p make a vector *ValPixelp(n)*. The mean value of this vector is calculated:

$$MeanValPixel(p) = \frac{1}{n}\sum_{i=1}^{n} ValPixel_p(i)$$

The standard deviation *STD(p)* is also calculated:

$$STD(p) = \frac{1}{n}\sqrt{\sum_{i=1}^{n}\left[ValPixel_p(i) - MeanValPixel(p)\right]^2}$$

The values $ValPixel_p(i)$ that deviate from the average by more than twice the *STD(p)* are rejected. Finally, the pixel value in the map *ValPixel(p)* is the average of the value fulfilling the following condition:

$$MeanValPixel(p) - 2 \times STD(p) < ValPixel_p(i) < MeanValPixel(p) + 2 \times STD(p)$$

This statistic approach is repeated for all the pixels, resulting in the complete map in the grey scale. The map of standard deviation is also obtained.

5.3.4 Calibration

The position dF_x of the flux gauge with respect to the black band on the bar is known and unchanged, as well as its distance dF_y from the bottom edge of the image. Therefore, the position $[X_{flux}(n), Y_{flux}]$ of the flux gauge in the corrected image n is derived from the location $X_{max}(n)$ of the black band in the corresponding image using a straightforward calculation:

$$\begin{cases} X_{flux}(n) = X_{max}(n) + dF_x \\ Y_{flux} = dF_y \end{cases}$$

The flux density measured by the flux gauge during the scanning is a function of time: $F_{measured}(t)$. The initial time is defined so that $F_{measured}(0)$ is the maximum value of $F_{measured}(t)$. The time scale is offset accordingly.

The n grey values corresponding to all the n positions of the flux gauge during the scanning are extracted from the map and expressed as a discrete function of space along the X axis: $ValPixel(x_n)=ValPixel(X_{flux}(n),Y_{flux})$. The initial time is attributed to the maximum value of $ValPixel(x_n)$. The discrete values of *ValPixel* are then reported to the time scale using the frame rate fps: the time between two successive values $ValPixel(x_i)$ and $ValPixel(x_{i+1})$ is 1/fps.

Finally, the values *ValPixel* are interpolated according to the time scale of $F_{measured}$ to obtain two vectors of same length l.

The calibration factor (or gain) G of the camera is determined by minimizing the cost function:

$$Cost(G) = \sqrt{\sum_{i=1}^{l} [G \times ValPixel(t_i) - F_{measured}(t_i)]^2}$$

The flux map is obtained from the grey map by multiplying the values by the gain G. As an example, the data resulting from the testing of the moving bar have been processed according to the method presented above. In this experiment, a single heliostat was focusing at the Next-CSP receiver central point. Figure 11 shows the results of the processing.

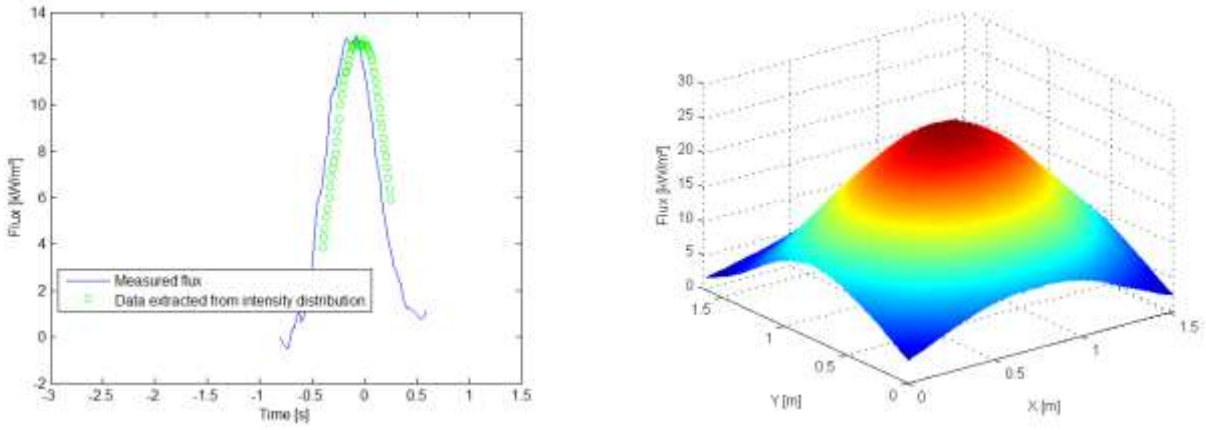

a) b)

Figure 11. Calibration and flux mapping; a) Time series $F_{measured}$ (in blue full line, left) and *ValPixel* (in green circles, right); b) Resulting flux map

5.3.5 Total incident power

The total solar power entering into the receiver is derived from the flux map by integrating the values of flux over the area of the receiver aperture. Numerical integration is made using the cell size of the grid on the flux map, which is 2.34 mm x 2.34 mm. The actual shape and size of the aperture are projected on the flux map to determine which cells are considered. The resulting total power is calculated as follows:

$$P_{solar-in} = \sum_{cells} [Flux(cell_i) \times Area(cell_i)]$$

In the example used to illustrate the method (Fig. 11), the projected aperture on the flux map (corresponding to the shape of the Next-CSP receiver) is shown in Figure 12 and the corresponding total input power is 24.3 kW.

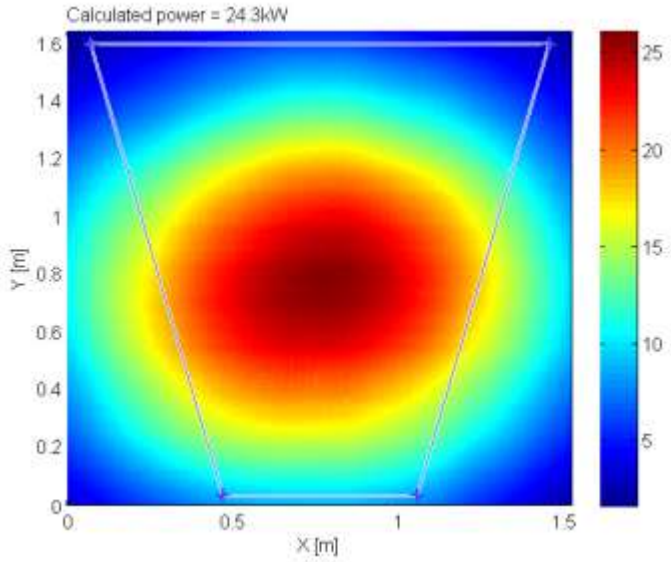

Figure 12. Projected aperture on the flux map (highlighted). Input power is 24.3 kW.

6. Results

Due to the absence of the solar receiver behind the moving bar, the results presented below are limited to two heliostats. Two aiming points, one for each heliostat, are defined. They are located 50 cm at the East and at the West of the Next-CSP receiver central point. This simulates an aiming strategy and prevents the protection from overheating.

The results are presented through the different steps on the software user interface.

Figure 13 presents the software user interface when it is launched.

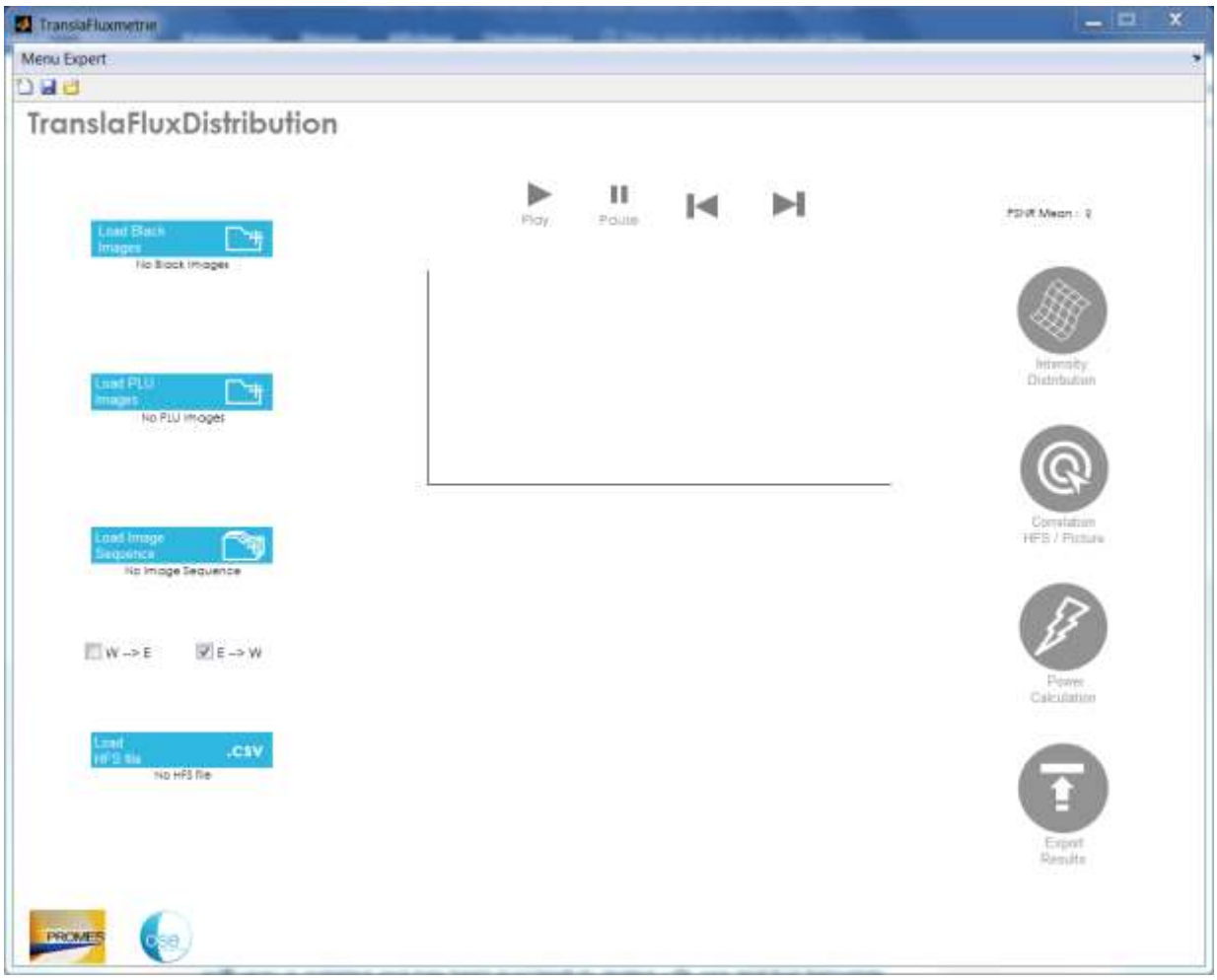

Figure 13. Software user interface when launched

After loading the black and flat pictures, the image sequence of the moving bar is loaded. Then we choose the direction (from West to East or East to West) and load the flux sensor file. Figure 14 shows the interface after clicking on the “Play” button and pausing it.

Figure 14. Software user interface when all files are loaded and the Play button is clicked

The PSNR is calculated after loading the black and flat images and the image sequence. We can see in this example that the PSNR value is equal to 55.15, which means that the noise and the bias are correctly removed.

After the video is completed, one can derive the intensity distribution, the correlation between the heat flux sensor and the intensity, and decide where to calculate the power in the reconstructed flux distribution (Figure 15).

Finally, we can export the following results after entering the solar irradiance during the experiment.

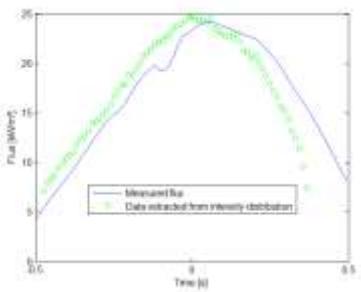

Correlation between heat flux sensor and intensity

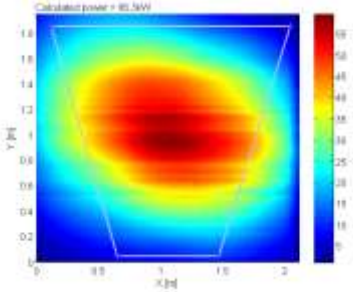

Flux distribution with calculated power in delimited frame

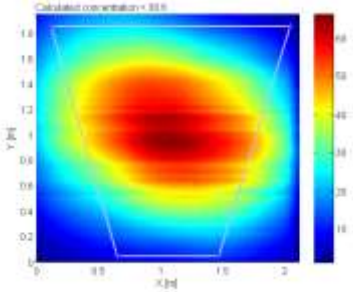

Concentration distribution with calculated concentration in delimited frame

Figure 15. The steps of the flux distribution measurement using two heliostats

7. Conclusion

The solar field is fully operational for the Next-CSP experiment. Indeed the 30 heliostats presenting a double focal spot have been readjusted by means of an optimization procedure based on a convolution-projection optical model and a deterministic algorithm.

An aiming point strategy tool has been developed to spread the flux distribution on the solar receiver in order to avoid hot spots and heat up the particles uniformly in all the tubes.

A new flux measurement system (moving bar, CMOS camera, heat flux sensor, post-processing software) was designed, manufactured and installed. It has been successfully tested with one and two heliostats. Therefore, the measurement method and post treatment software are considered as fully operational.

8. References

[1] A. Salomé & al., Solar Energy 94, 352-366 (2014).

[2] F.J. Collado, A. Gómez and J. Turégano, Journal of Solar Energy 37, 215-234 (1986)

[3] PROMES-CNRS, MESO-STAR SAS. SOLSTICE, SOLar Simulation Tool In ConcEntrating optics, version 0.7.1 (2017), France, https://www.meso-star.com/projects/solstice.html https://www.labex-solstice.fr/logiciel-solstice.html